# Printable Perovskite Diodes for Broad-Spectrum Multienergy X-Ray Detection

*Babar Shabbir,* Jae Choul Yu, Tharindu Warnakula, R. A. W. Ayyubi, James A. Pollock, M. Mosarof Hossain, Jueng-Eun Kim, Nasiruddin Macadam, Leonard. W. T. Ng, Tawfique Hasan, Doojin Vak, Marcus J. Kitchen, and Jacek J. Jasieniak**

**Multienergy X-ray detection is critical to effectively differentiate materials in a variety of diagnostic radiology and nondestructive testing applications. Silicon and selenium X-ray detectors are the most common for multienergy detection; however, these present poor energy discrimination across the broad X-ray spectrum and exhibit limited spatial resolution due to the high thicknesses required for radiation attenuation. Here, an X-ray detector based on solution-processed thin-film metal halide perovskite that overcomes these challenges is introduced. By harnessing an optimized n-i-p diode configuration, operation is achieved across a broad range of soft and hard X-ray energies stemming from 0.1 to 10's of keV. Through detailed experimental and simulation work, it is shown that optimized $Cs_{0.1}FA_{0.9}PbI_3$ perovskites effectively attenuate soft and hard X-rays, while also possessing excellent electrical properties to result in X-ray detectors with high sensitivity factors that exceed $5 \times 10^3$ μC $Gy_{Vac}^{-1}$ $cm^{-2}$ and $6 \times 10^4$ μC $Gy^{-1}$ $cm^{-2}$ within soft and hard X-ray regimes, respectively. Harnessing the solution-processable nature of the perovskites, roll-to-roll printable X-ray detectors on flexible substrates are also demonstrated.**

## 1. Introduction

Since the first use of X-rays to study material structures in the early parts of the 20th century,[1] their use in the modern era has addressed a plethora of challenging detection problems, including the diagnosis of diseases in humans, detection of metal explosives, and identification of physical food contaminants. The most common approach to X-ray detection is through a single energy X-ray window technology, which typically operates in the hard X-ray region (≈10 to 100 keV). This is ideal for hard materials, such as high-density bones, ceramics, metals, and stones, which effectively absorb hard X-rays. However, for relatively low-density objects that have small X-ray attenuation coefficients in this spectral region, limited information can be extracted. For example, the four most abundant elements in living

---

B. Shabbir, J. C. Yu, T. Warnakula, M. M. Hossain, J.-E. Kim, J. J. Jasieniak
Department of Materials Science and Engineering
Monash University
Clayton, Victoria 3800, Australia
E-mail: babar.shabbir@monash.edu; jacek.jasieniak@monash.edu

B. Shabbir, J. C. Yu, T. Warnakula, J. J. Jasieniak
ARC Centre of Excellence in Exciton Science
Monash University
Clayton, Victoria 3800, Australia

R. A. W. Ayyubi
Department of Physics
University of Illinois at Chicago
Chicago, IL 60607, USA

The ORCID identification number(s) for the author(s) of this article can be found under https://doi.org/10.1002/adma.202210068.

**DOI: 10.1002/adma.202210068**

J. A. Pollock, M. J. Kitchen
School of Physics and Astronomy
Monash University
Clayton, Victoria 3800, Australia

M. M. Hossain
Department of Neuroscience, Central Clinical School
Monash University
Melbourne, Victoria 3004, Australia

J.-E. Kim, D. Vak
CSIRO Manufacturing
Clayton, Victoria 3168, Australia

N. Macadam, Leonard. W. T. Ng, T. Hasan
Cambridge Graphene Centre
University of Cambridge
CB3 0FA, Cambridge, UK

Leonard. W. T. Ng
School of Materials Science and Engineering
Nanyang Technological University
Singapore 639798, Singapore

organisms, namely, hydrogen, carbon, oxygen, and nitrogen possess *K*-edges that are below 1 keV, making them practically invisible to high-energy X-ray ex vivo imaging.[2] This further impacts the detection of such materials in heterogenous substances in which both low- and high-density components exist.[3] These challenges can be addressed by studying samples through multi X-ray energies that discriminate structure based on the distinct attenuation coefficients of materials across a broad spectral region.[4]

Dual energy detection is one sub-set of this approach that typically works by using two images of the same object at different X-ray energies. These images can then be combined to differentiate low- and high-density materials. Modern advances in dual energy X-ray detection have explored various kinds of detectors, ranging from computer radiography systems to modern flat panel amorphous silicon (a-Si) or amorphous selenium (a-Se) arrays.[4] Among these, a-Se X-ray detectors are the most commonly used for direct conversion-type dual energy imaging, including chest imaging, and bone and breast density quantification.[5] However, in specific cases, such as when identifying angiogenesis (an indicator of malignant tumors) in the breast, digital mammography requires X-ray energies greater than 33 keV. This is above the K-shell binding energy of iodinated contrast agent.[5] This limitation arises because a-Se detectors exhibit low attenuation efficiencies at these higher energies,[5a] which necessitates thick a-Se films (≈500 µm) to sufficiently attenuate hard X-rays beyond 30 keV. As a result, large, applied voltage biases of >5 kV are required to enable effective transport of the electrical carriers within the detectors. This poses significant limitations to the practical operation of the X-ray detectors, which are based on thin-film transistor architectures, while also introducing resolution limitation due to the oblique entry of X-rays.[6]

Recently, metal halide perovskites have emerged as very promising materials for use in X-ray detection due to their excellent X-ray attenuation characteristics, large mobility-lifetime product ($\mu\tau$), tuneable bandgap, and inexpensive synthesis.[7] These advantageous properties result in high sensitivities in the range of $10^2$ to $10^6$ µC Gy$^{-1}$ cm$^{-2}$ for perovskite X-ray detectors based on lead and nonlead poly- and single-crystal absorbers,[8] significantly higher than that of commercial a-Se detectors (20 µC Gy$^{-1}$ cm$^{-2}$). Despite these early promises, perovskites have only been demonstrated for hard X-ray detection.[7a,8,9] Moreover, the demonstrated direct detectors have been typically at small prototype scales of a few millimeters to centimeters.[8,9] In this work, we address both these factors by developing high sensitivity, large area perovskite-based X-ray detectors that can be used across a broad spectrum of X-ray energies. This represents a significant step forward toward detailed imaging of heterogenous substances.

## 2. Material Characterization and Device Configuration

We use $Cs_{0.1}FA_{0.9}PbI_3$ metal halide perovskite because of its improved stability than analogs containing methyl ammonium (MA), such as $MAPbI_3$.[10] **Figure 1**a shows the X-ray diffraction (XRD) patterns of the $Cs_{0.1}FA_{0.9}PbI_3$ perovskite films. The absence of peaks $2\theta = 11.7°$ and $2\theta = 15.9°$ suggests that the films do not feature phase-segregated hexagonal nonperovskite $\delta$-phases of $FAPbI_3$ and $CsPbI_3$, respectively, and instead are composed of pure black-phased perovskite.[11] To assess the prospects of $Cs_{0.1}FA_{0.9}PbI_3$ film for X-ray attenuation, we use the National Institute of Standards and Technology (NIST) photon cross-section database to calculate its X-ray attenuation coefficient (Figure 1b).[12] In both soft and hard X-ray regions, the attenuation coefficient of $Cs_{0.1}FA_{0.9}PbI_3$ is found to be higher than a-Se and most other metal halide perovskites (Figure S1a, Supporting Information). The presence of lead ($Z = 82$) and the high gravimetric density of ≈4.33 g cm$^{-3}$ supports a very high X-ray attenuation coefficient $\mu$ for $Cs_{0.1}FA_{0.9}PbI_3$ (i.e., $\mu = \rho Z^4/AE^3$, where $Z$ is the atomic number of the absorbing atoms, $E$ is the X-ray incident energy, $\rho$ is the density, and $A$ is the atomic mass).[7a] Importantly, when comparing the attenuation efficiencies at both the soft and hard X-ray regions, $Cs_{0.1}FA_{0.9}PbI_3$ is among the most effective in absorbing X-ray photons across both the regions (Figure 1c). For a representative 800 nm absorber thickness, it can achieve >90% attenuation in the soft region and a modest ≈4% within the hard region. We note that although $MAPbI_3$ shows comparable values, it may not be durable for long-term operation.[9a]

The effectiveness of $Cs_{0.1}FA_{0.9}PbI_3$ films in attenuating X-rays is explored both through direct and indirect detection approaches. At the simplest level, the indirect detection of hard X-rays is achieved through the use of a perovskite film directly as scintillator, which converts X-rays into visible photons that are subsequently detected by a photodiode array. This approach leverages the intrinsic defect-tolerant structure of the perovskite, which minimizes nonradiative recombination and further provides high fluorescence quantum yields of the perovskite thin films.[13] The X-ray image of an LM2907N voltage multiplier chip (Figure 1d) is taken using such an indirect conversion approach (see Section A-i, Supporting Information), showing the buried circuitry in the marked area (Figure 1e). To determine the spatial resolution of this imaging technique, a Pearson fit of the line spread function was carried out (Figure 1f), yielding a maximum spatial resolution of 67.5 µm. While the indirect approach offers simple detector integration, they only allow limited spatial and temporal resolutions.[9a,14]

Direct conversion-type detectors provide considerable fabrication and resolution benefits over such an indirect conversion-type detector because of their simpler device design and the lower thickness requirement of the X-ray detecting material.[7a,8,9] When X-rays with energies up to several hundred keVs interact with a suitable absorbing material, they generate free charge carriers due to ionization through the photoelectric effect. This permits direct X-ray detection whereby these carriers are collected as a photocurrent within a suitable optoelectronic device architecture. We have assessed a number of device structures for the direct conversion of X-rays using the $Cs_{0.1}FA_{0.9}PbI_3$ absorber (see Section A-ii, Supporting Information). Of these, the n-i-p diode configuration is found to be the most promising due to its well-aligned energy level structure (see Section A-iii, Supporting Information). While various

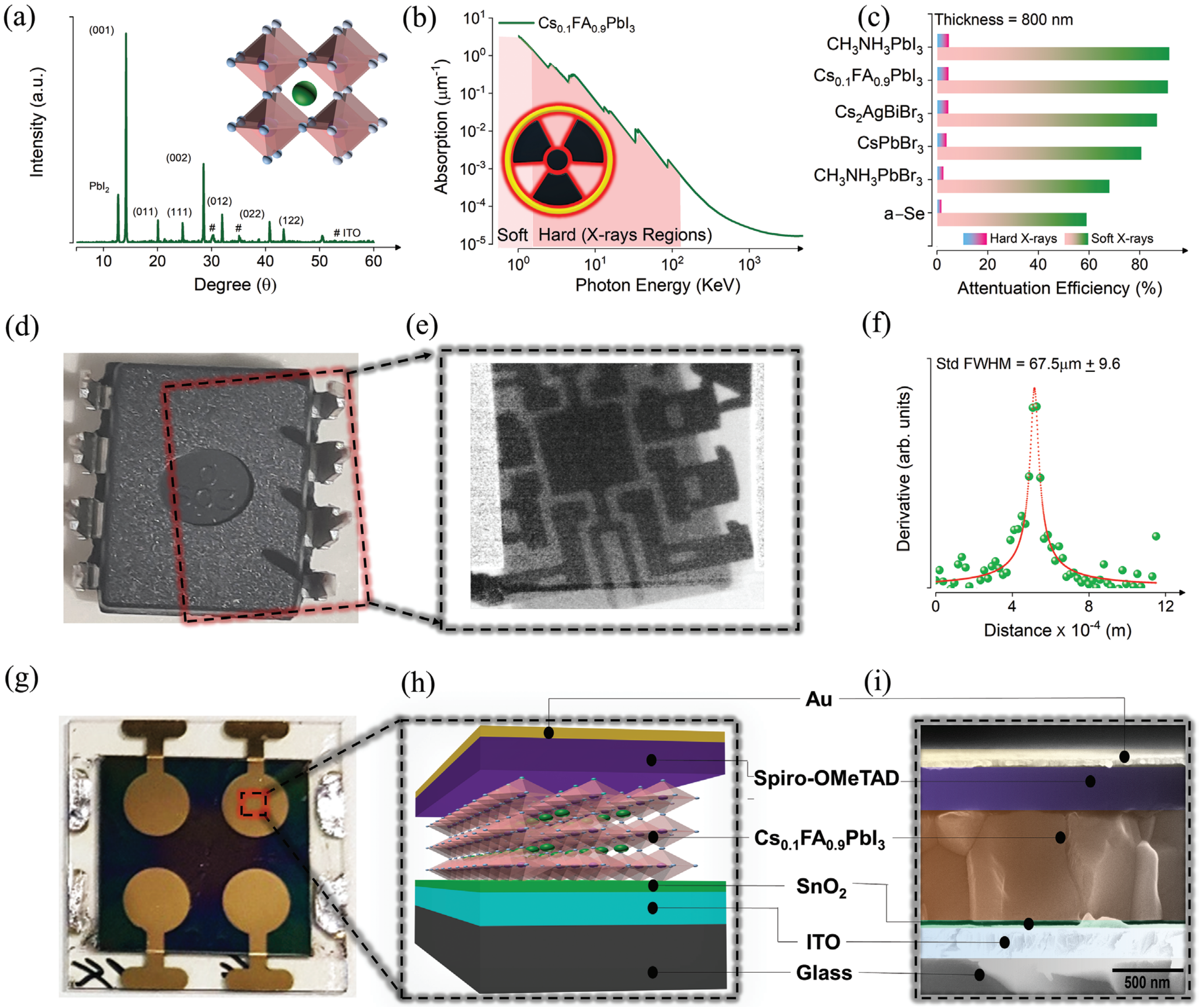

**Figure 1.** Material characterization and device configuration. a) The XRD pattern and associated perovskite crystal structure (inset) of $Cs_{0.1}FA_{0.9}PbI_3$. b) Attenuation coefficient of $Cs_{0.1}FA_{0.9}PbI_3$ in soft (0.1 keV < photon energy < 10 keV) and hard (10 keV < photon energy < 100 keV) X-ray regions. c) Attenuation efficiency comparison of high-performing perovskites at 800 nm thickness in soft (1 keV) and hard (10 keV) X-ray ranges. d) Photograph of a multiplier chip (Area ~ $4 cm^2$) and e) the corresponding X-ray image taken by using indirect conversion. f) The Pearson VII fit of the line spread function where the full-width half-maximum defines the spatial resolution of $Cs_{0.1}FA_{0.9}PbI_3$ as 67.5 µm. g) Actual photograph of a device on a 1 × 1 in. glass substrate with representative 2 × 2 pixels. h) Schematic showing the n-i-p diode device configuration with the corresponding i) false-color cross-section SEM micrograph of a completed glass (1.1 mm)/ITO (≈200 nm)/$SnO_2$ (≈30 nm)/$Cs_{0.1}FA_{0.9}PbI_3$ (≈800 nm)/Spiro-OMeTAD (≈200 nm)/Au (≈80 nm) device.

perovskite thicknesses have been explored in this work, a typical device is shown in Figure 1g featuring a ≈800 nm thick polycrystalline $Cs_{0.1}FA_{0.9}PbI_3$ film sandwiched between $SnO_2$ (≈30 nm) and Spiro-OMeTAD (≈200 nm) charge selective layers. The device configuration (Figure 1h) and typical cross-sectional scanning electron microscope (SEM) image (Figure 1i) show the n-i-p diode device with gold (top) and indium tin oxide (ITO, bottom) electrodes, consistent with that of high-efficiency solar cells.[10] We adopt this device architecture to directly leverage the tremendous recent advances in interfacial and device engineering for broad-spectrum multienergy X-ray detection.

## 3. Soft and Hard X-Ray Detectors

To achieve optimal performance in both soft and hard X-ray regions, the thickness of the absorber material needs to be carefully selected to balance between soft and hard X-ray absorption. This arises because the lower attenuation coefficient in the hard X-ray region necessitates thicker films compared to those optimized purely for the soft X-ray regime. To probe these performance limits, we first consider the predicted sensitivity ($S$) factors. Theoretically, $S \propto \eta_x \eta_m \eta_{cc}$, where $\eta_x$ is the absorption efficiency, $\eta_m$ is the material-dependent conversion efficiency, and $\eta_{cc}$ is the charge collection efficiency.[15] These

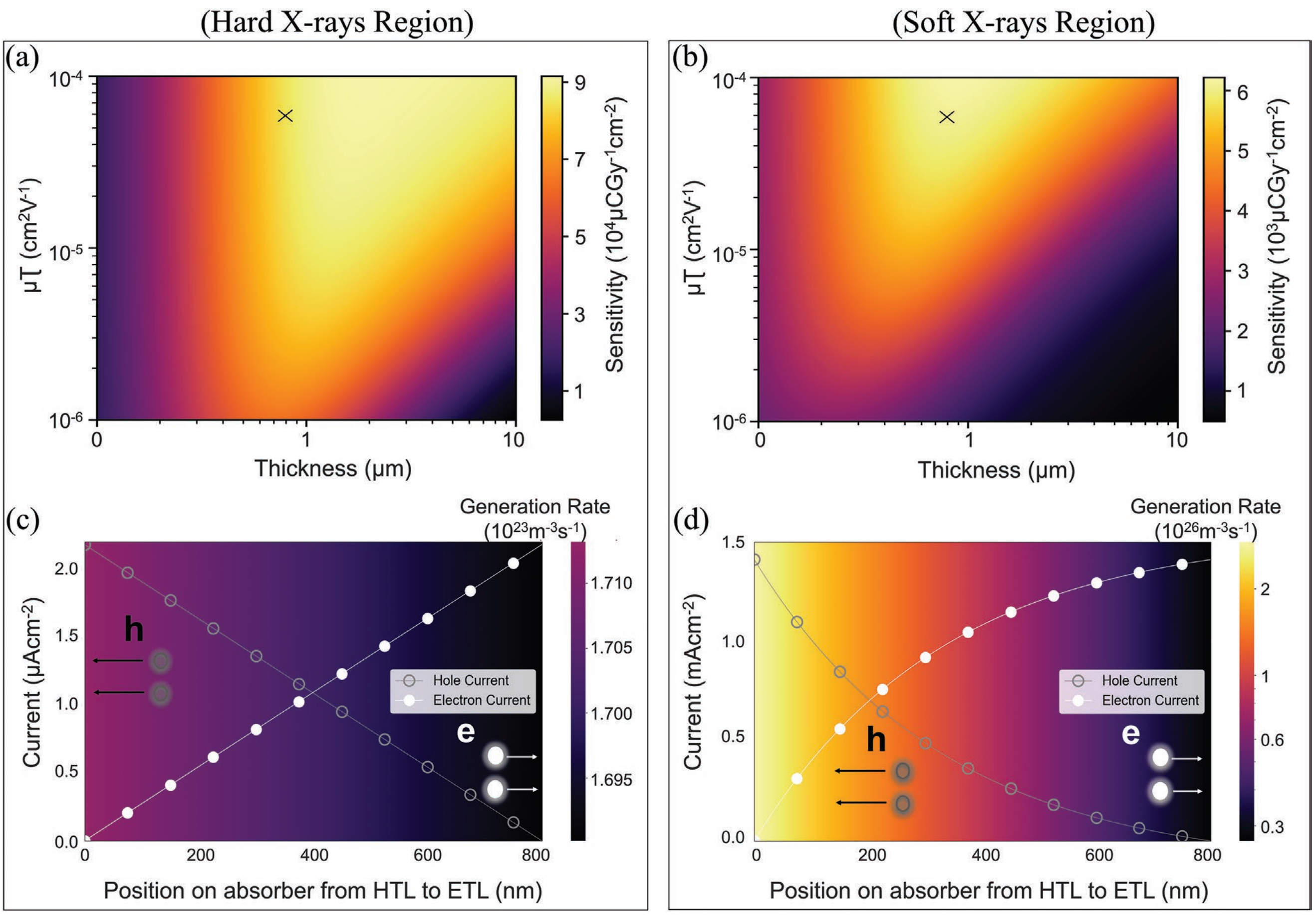

**Figure 2.** Optimizing broad-spectrum multienergy X-ray detection. Simulated sensitivity of perovskite diodes as a function of thickness and $\mu\tau$ product in the a) hard and b) soft X-rays regimes. The hole and electron currents across the perovskite layer as determined by finite element simulations for c) hard X-rays at 20 keV with a dose rate of 235 mGy s$^{-1}$ and d) soft X-rays at 1 keV with a dose rate of 110 mGy s$^{-1}$. The left and right edges of the figure represent the hole transport layer (HTL) and ETL boundaries, respectively.

interdependent factors dictate that $S$ is governed by the extent of absorption, the photon energy, and the specific $\mu\tau$ product ($\mu$ being the carrier mobility and $\tau$ being its lifetime) within the absorbing layer (see Section B-i, Supporting Information). Of these, the $\mu\tau$ product defines the effective distance that carriers can travel before recombining under a given electric field. It provides a direct gauge into the extraction depth of carriers within a semiconducting material, with larger $\mu\tau$ values enabling enhanced charge collection efficiency. Studies on metal halide perovskites have shown that single crystals demonstrate large $\mu\tau$ products on the order of ≈ $10^{-2}$ cm$^2$ V$^{-1}$, while comparatively lower values of ≈ $10^{-4}$ to $10^{-7}$ cm$^2$ V$^{-1}$ are found in polycrystalline perovskite films.[7d,10,16] This difference is ascribed to the higher trap densities and lower mobilities in the thin-film-structured perovskites.[17]

As a first approximation, it can be considered that $\mu_e = \mu_h$ for organic–inorganic lead halide perovskites.[15a,16] Within this approximation, the $S$-values across both soft and hard X-rays regions have been simulated within a thickness range of 0.2–5 µm under an electric field of 1 mV µm$^{-1}$ and a characteristic $\mu\tau$ range of $10^{-6}$ to $10^{-4}$ cm$^2$ V$^{-1}$ to reflect practical limits of typical perovskite thin films (see **Figure 2**a,b).[10,16] The results indicate that $S$-values are initially enhanced with increasing thickness, reaching a saturation point of ≈ $8 \times 10^4$ µC Gy$^{-1}$ cm$^{-2}$ for hard X-rays and ≈$5.5\times10^3$ µC $\mathrm{Gy}_{\mathrm{Vac}}^{-1}$ cm$^{-2}$ for soft X-rays. This trend reflects the progressive increase in X-ray-induced carrier generation arising from absorption. Across both energy regions, a reduction in $S$-values is also predicted for higher perovskite thicknesses, which is exacerbated at lower $\mu\tau$ values. This observation reflects the enhanced carrier recombination dynamics beyond the practical diffusion limits of charge carriers. For the $\mathrm{Cs_{0.1}FA_{0.9}PbI_3}$ thin films that have been used in our X-ray detectors, a $\mu\tau$ value of ≈5 × $10^{-5}$ cm$^2$ V$^{-1}$ has been reported.[16,18] The simulated $S$-values for this $\mu\tau$ indicate that a perovskite film thickness of ≈800 nm is considered optimal to provide balanced performance across both hard and soft X-ray regimes. Importantly, this is within the current practical thickness limits that high-quality solution-processed perovskites thin films can be fabricated.

To further understand the working priniples of the X-ray detectors across both hard and soft X-ray regimes, drift-diffusion simulations were performed to calculate the carrier generation rates across such 800 nm thick perovskite detectors (see Section B-ii, Supporting Information). Figure 2c indicates an almost homogenous carrier generation profile across the perovskite under hard X-ray exposure due to the limited

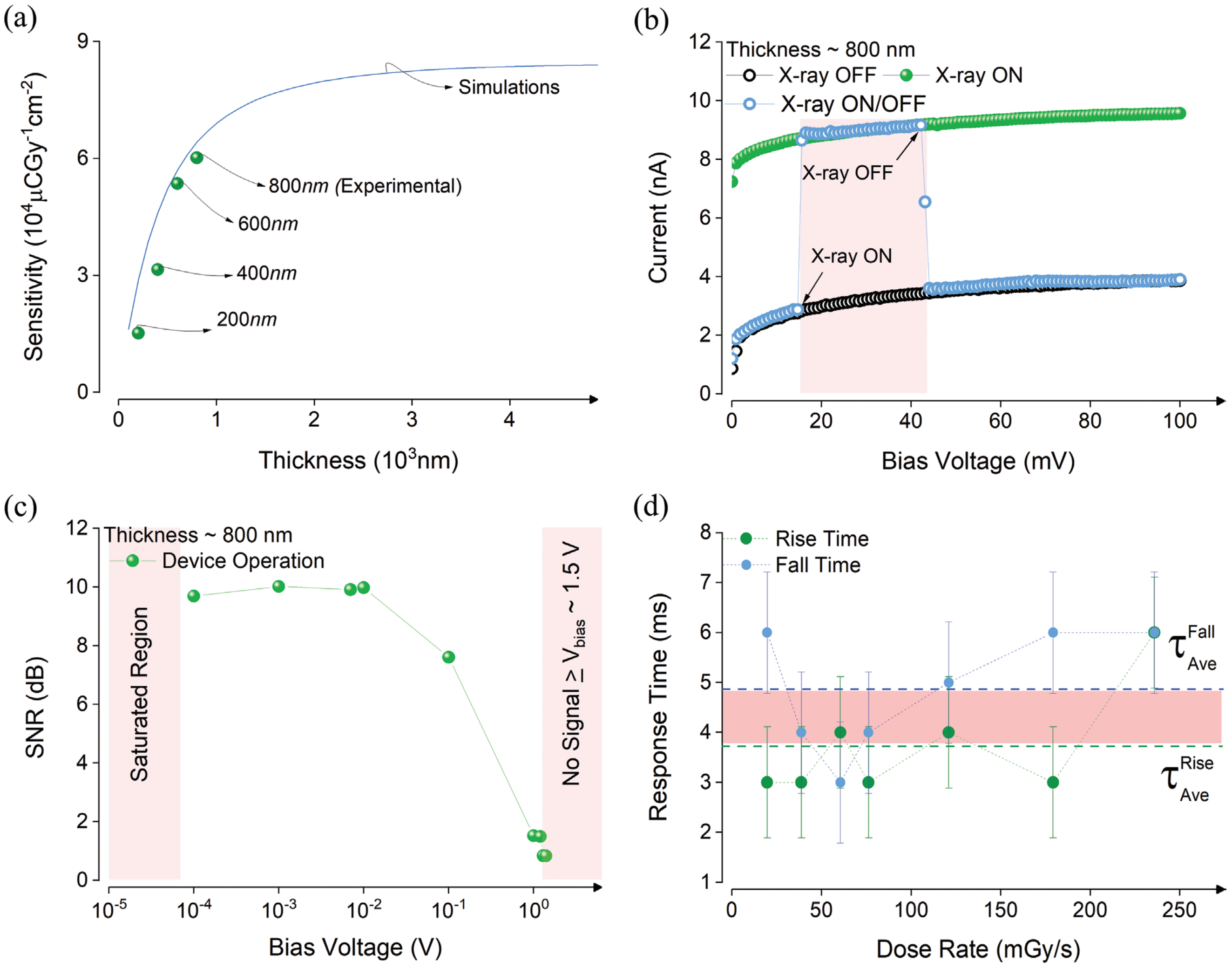

**Figure 3.** Performance in hard X-ray region. a) The experimental and theoretical *S* values comparison as a function of perovskite thickness within the hard X-ray region. The results indicate that *S*-values are initially enhanced with increasing thickness, reaching a saturation point of ≈$8 \times 10^4$ µC Gy$^{-1}$ cm$^{-2}$. The experimental results are in good agreement with predictions. b) The current–voltage (*I–V*) curve of an n-i-p device shows current under X-ray OFF, ON, and ON/OFF conditions. c) The SNR is plotted at several $V_{\mathrm{bias}}$ and 0.15 µGy s$^{-1}$, indicating the device working range. d) The average rise and fall times at several dose rates are estimated to be ≈4 and 5 ms, respectively.

absorption coefficient in this region. As a result, the electron and hole currents across the device vary linearly. These trends imply that the perovskite thickness could be further increased to generate more current without sacrificing charge extraction efficiency. In contrast, Figure 2d shows that the generation rate across the device decreases exponentially in the soft X-ray regime as governed by the Beer–Lambert law. In this instance, the electron and hole currents reach saturated values toward the electron transport layer (ETL), which represents the back interface of the device. This suggests that the device is operating at, or near, optimal charge extraction conditions. Further thickening of the perovskite layer will not significantly increase the output current because the limited mobilities will induce carrier recombination.

To verify the predicted X-ray performance characteristics, devices with $\mathrm{Cs_{0.1}FA_{0.9}PbI_3}$ films of several thicknesses up to 800 nm have been compared (see Section C-i, Supporting Information). Here, the experimental *S* has been determined simply as $S = J_\mathrm{p}/D$, where $J_\mathrm{p}$ is the current density of the detector and *D* is the X-ray dose rate (see the Experimental Section). Under hard X-ray exposure, the obtained experimental sensitivities are found to progressively improve with increasing perovskite thickness, achieving a value of ≈ $6 \times 10^4$ $\mu$C Gy$^{-1}$ cm$^{-2}$ for 800 nm thick films (**Figure 3**a). The experimental results are in good agreement with predictions. Devices with thicker perovskite films have not been included here because these could not be fabricated without significant cracking, thus yielding poorly operating detectors.

Owing to the n-i-p design, the devices demonstrate a low dark current of few nanoamperes (≈2 nA at $V_{\mathrm{bias}} = 1$ mV). Such a low dark current is crucial to direct-type detectors as it i) mitigates shot noise ($I_\mathrm{n} = \sqrt{2qI_\mathrm{d}\Delta f}$, $q$ is an electron charge, $I_\mathrm{d}$ is the dark current, and $\Delta f$ is the bandwidth in Hertz), ii) increases the dynamic range of the detector, and iii) maximizes the temporal readout resolution and sensitivities.[9b,19] As a result, when the diode is exposed to X-rays at a small dose rate of 0.15 µGy s$^{-1}$, a fourfold increase in the current (≈8 nA) is observed (Figure 3b). A linear photocurrent dependence is observed with increasing dose rate of up to 0.9 μGy s$^{-1}$, with saturation being observed at higher dose values of >100 mGy s$^{-1}$ (see Section C-ii, Supporting Information).

To determine the device's signal strength and working range, the signal-to-noise or SNR ratio is calculated.[20] For hard X-rays under the lowest dose rate of ≈0.15 μGy s$^{-1}$, strong SNRs of ≈10 dB are observed at $V_{\text{bias}} < 100$ mV (Figure 3c). This subsequently decreases at higher voltages until the device effectively stops working at a $V_{\text{bias}} > 1.5$ V due to increased dark current. At higher exposures, the SNR is further enhanced due to the increased X-ray-induced current, e.g., an SNR of ≈45 dB is achieved at a dose rate of 120 mGy s$^{-1}$ (see Figure S6b, Supporting Information). The strong signal strength of the perovskite devices is consistent with their high X-ray attenuation coefficient, low nonradiative recombination, and excellent charge carrier transport properties.[8,9]

Another important parameter of the hard X-ray detector is its response time. Generally, the state-of-the-art perovskite-based X-ray detectors demonstrated a response time in the order of seconds to milliseconds.[7c,d,g,21] The X-ray detectors based on polycrystalline films are limited by the hindered transport characteristics and enhanced recombination stemming from grain boundaries to yield typical response values of 10's of ms.[7g] The perovskite diodes explored here exhibit very short average response times of ≈3–5 ms (Figure 3d). The short response time observed here indicates effective carrier transport, low levels of trapping, and good carrier extraction.[22] Moreover, these values lend themselves to detectors that can provide near real-time detection at ≈100's Hz scan rates.

Within the soft X-ray regime, the experimentally obtained sensitivity of $\approx 5\times 10^{3}$ $\mu\text{C}\, Gy_{\text{Vac}}^{-1}\, \text{cm}^{-2}$ for a near-optimal 800 nm perovskite thickness is in good agreement with predictions (**Figure 4**a). Exposure of the devices to soft X-rays with a photon energy of 700 eV and flux of $3.98 \times 10^{11}$ ph s$^{-1}$ is found to induce a 1000-fold increase over the dark current at mV scales (see Section D-i, Supporting Information). The SNRs of the device at various voltages are shown in Figure 4b. Compared to hard X-rays, the SNR values of the diodes at ≈1 mV reach almost 60 dB when exposed to X-ray photons of energy 1.2 keV with a flux of $2.63 \times 10^{11}$ph s$^{-1}$. Moreover, measurements at 2.0 keV yield an SNR strength of > 40 dB at the relatively low flux of $2.6 \times 10^{10}$ ph s$^{-1}$. This suggests efficient detection of soft objects is possible, even under weak X-ray sources. These results validate the excellent sensitivity of these devices toward soft X-rays, with their performance being, to the best of our knowledge, the highest among all reported soft X-ray detectors (see Table S3, Supporting Information).[22,23] The excellent response characteristics are directly attributed to the efficient transport properties of the perovskite, its large soft X-ray attenuation coefficient, and the high flux of the synchrotron X-ray beam.

An important aspect of X-ray detectors is the efficient discrimination between small or large changes in photon flux. Here, the X-ray flux at a fixed photon energy of 700 eV has been controlled by changing the beamline slit size to achieve flux levels between 0 and $5.8 \times 10^{12}$ ph s$^{-1}$ (Figure 4c). At $V_{\text{bias}} = 1$ mV, the diode successfully detects photons with large dynamic photocurrent responses and a linear correlation to flux levels with no saturation at the flux levels studied here (see Figure S9, Supporting Information). To further demonstrate the ability of this device to detect minute changes in flux, the device performance is measured under the synchrotron beam with an exposure area of 1 mm$^2$ with and without a mesh filter, giving $3.57 \times 10^{11}$ and $3.98 \times 10^{11}$ ph s$^{-1}$, respectively (inset of Figure 4d). The diode is found to readily detect this minor signal (Figure 4d). These results show that the perovskite X-ray detectors can efficiently detect soft objects over large flux ranges to make them attractive candidates for broad-spectrum multi-energy detectors. A proof-of-concept 4 pixel device providing broad-spectrum multienergy detection is included in Section E in the Supporting Information.

## 4. Flexible and Printable Perovskites-Based X-Ray Diodes

One of the key advantages of perovskites is in their potential for being implemented within large-scale devices through roll-to-roll (R2R) deposition approaches. **Figure 5**a schematically illustrates the successive deposition of an n-i-p diode on a flexible polyethylene terephthalate substrate with an ITO electrode. To demonstrate a low-cost and fully printed prototype device, the typically employed gold top electrode is replaced with a printed carbon electrode. These devices are fabricated using a custom-made slot die on a commercial R2R coater in a vacuum-free environment (see the Experimental Section for details).

The printed perovskite diodes are considered here as radiation detectors. To mimic the detector's positioning placements on chest level, wrist, and fingers, characteristic bending angles of 0°, ≈45°, and ≈90°, respectively, are considered (Figure 5b–d). At these bending angles, the devices demonstrate more than twofold counts per second (cps) enhancements in output signals under X-ray exposure. The flexible devices are found to exhibit high signal levels of ≈ $1.6 \times 10^{9}$ cps (on average) at modest bias voltages of 10 mV. Furthermore, comparable net signals ($\text{cps} = \text{cps}_{\text{X-ray ON}} - \text{cps}_{\text{X-ray OFF}}$) of ≈$10^{9}$ cps are recorded under 0°, ≈45°, and ≈90° device bending angles.

Bending of poorly bonded films on a flexible substrate can deteriorate the cps signal, even under a modest strain.[24] As such, large grain perovskite films are highly susceptible to crack formations under mechanical stress.[25] The 800 nm thick perovskite films explored here show negligible deterioration under ≈45° and ≈90° bending angles, with limited cycle testing further showing no discernible changes in device performance (see Section F, Supporting Information). These performance characteristics indicate suitability of these printed diodes as effective radiation detectors that may require flexible form factors and/or large scale.

## 5. Conclusion

Both soft and hard X-ray regimes provide important and differentiated spectroscopic prospects toward understanding complex heterogenous materials. While silicon and selenium detectors remain the archetypal candidates for X-ray detection, they cannot effectively operate across both the regimes

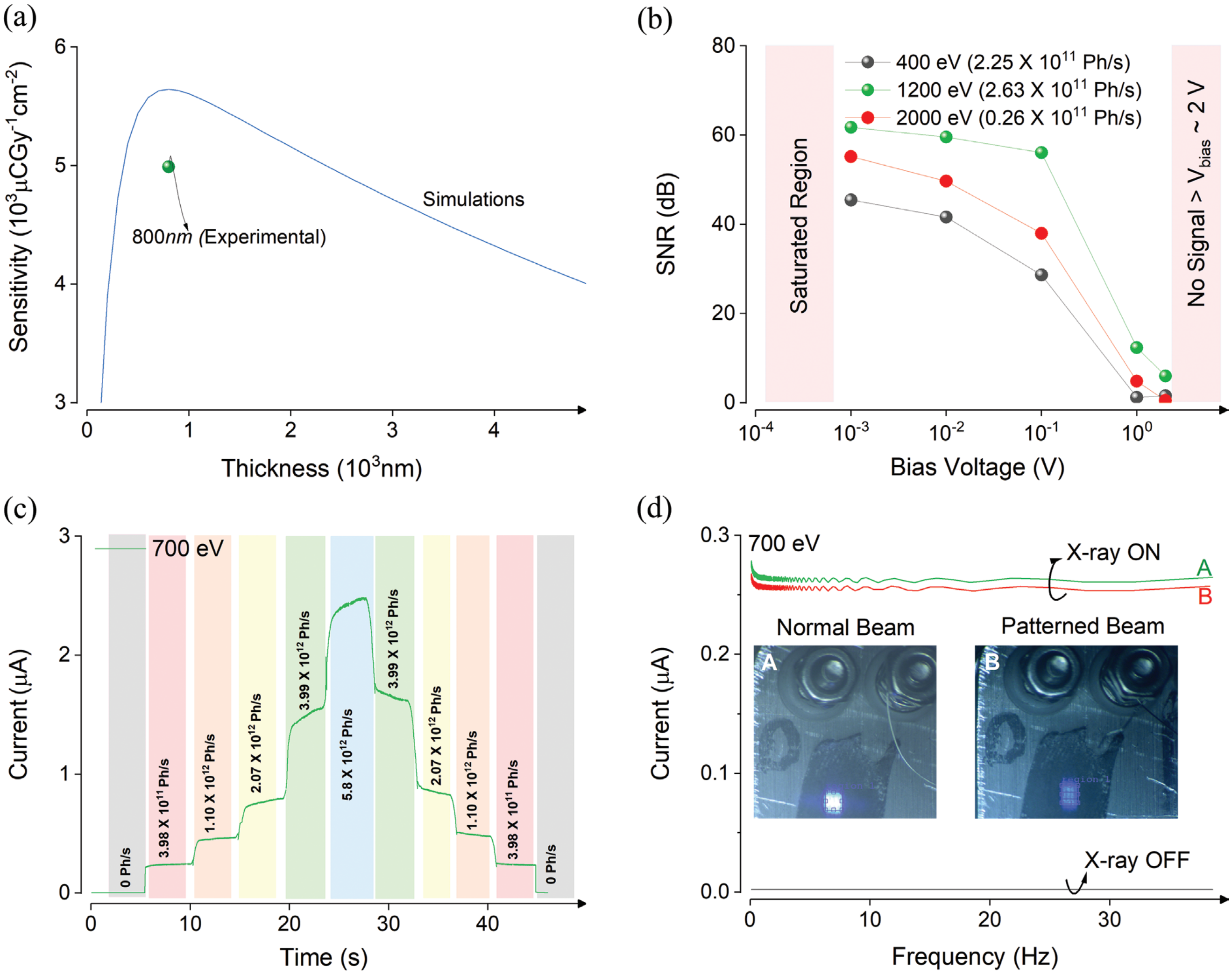

**Figure 4.** Performance in soft X-ray region. a) The experimental and theoretical *S* values as a function of perovskite thickness within the soft X-ray region. b) The SNR versus $V_{bias}$ under selected photon energy value and flux shows excellent operation of the devices at low biases. c) The current is recorded in real-time within changes in photon flux at a fixed photon energy of 700 eV. d) The current as a function of frequency indicates minimal dependency between performance and frequency (10 Hz range). Moreover, a comparison of the device response to minute changes in the flux value for a standard beam (A) and an attenuated patterned beam (B) is included. The actual photographs of these beams are shown as insets. These photos are taken by exposing the soft X-ray beam to phosphorous scintillators which are deposited on an insulating black tape attached to the sample *x–y* positioning stage. The beam area is 1 mm$^2$.

within a single device architecture. Here, we showcase that $Cs_{0.1}FA_{0.9}PbI_3$ metal halide perovskite can effectively absorb X-rays across both of these regimes due to their high attenuation coefficients. When incorporated into n-i-p diode configurations, we achieve high-performance values across these regimes, with sensitivities of up to ≈$5 \times 10^3$ µC $Gy_{Vac}^{-1}$ cm$^{-2}$ for soft X-rays and $6 \times 10^4$ µC Gy$^{-1}$ cm$^{-2}$ for hard X-rays. Detailed modeling validates that for solution-processed perovskite thin films, 800 nm thick layers provide nearly optimal performance across these regimes. Owing to their performance and multifaceted applicability, we anticipate that these printable, scalable, and flexible perovskite diode devices can provide a step-jump for imaging applications requiring broad-spectrum multienergy X-ray detection. Given the rapid response times and high sensitivities of these perovskite-based detectors, our work enables real-time detection and imaging opportunities of heterogenous substances.

## 6. Experimental Section

*Device Fabrication*: The devices were fabricated on ITO-coated glass substrates (13 Ω sq$^{-1}$) supplied by Kintec, which were used after being cleaned sequentially by sonicating for 10 min in deionized (DI) water, acetone, and isopropyl alcohol, drying under a stream of nitrogen gas, and then treating for 15 min under $O_2$-plasma (Harrick Plasma). A dilute $SnO_2$ (3 wt% in DI water) nanoparticle solution (80 µL) was spin-coated at 5000 rpm for 30 s onto the substrate and annealed at 150 °C for 30 min. The perovskite precursor solutions were prepared by 1.52 M of FAI, 0.08 M of CsI, and 1.6 M of $PbI_2$ in 1 mL of dimethylformamide/dimethyl sulfoxide (8:2 v/v) co-solvent. The prepared perovskite solutions (50 µL) were spin-coated onto the $SnO_2$-coated ITO substrate using a two-step method, first at 1000 rpm for 10 s, followed by 4000 rpm for 20 s. During the spin-coating step at 4000 rpm, diethyl ether (1 mL) was deposited onto the surface after a delay of 15 s, with the substrates then annealed at 150 °C for 10 min. The Spiro-OMeTAD solution was spin-coated onto the perovskite layer at 3000 rpm for

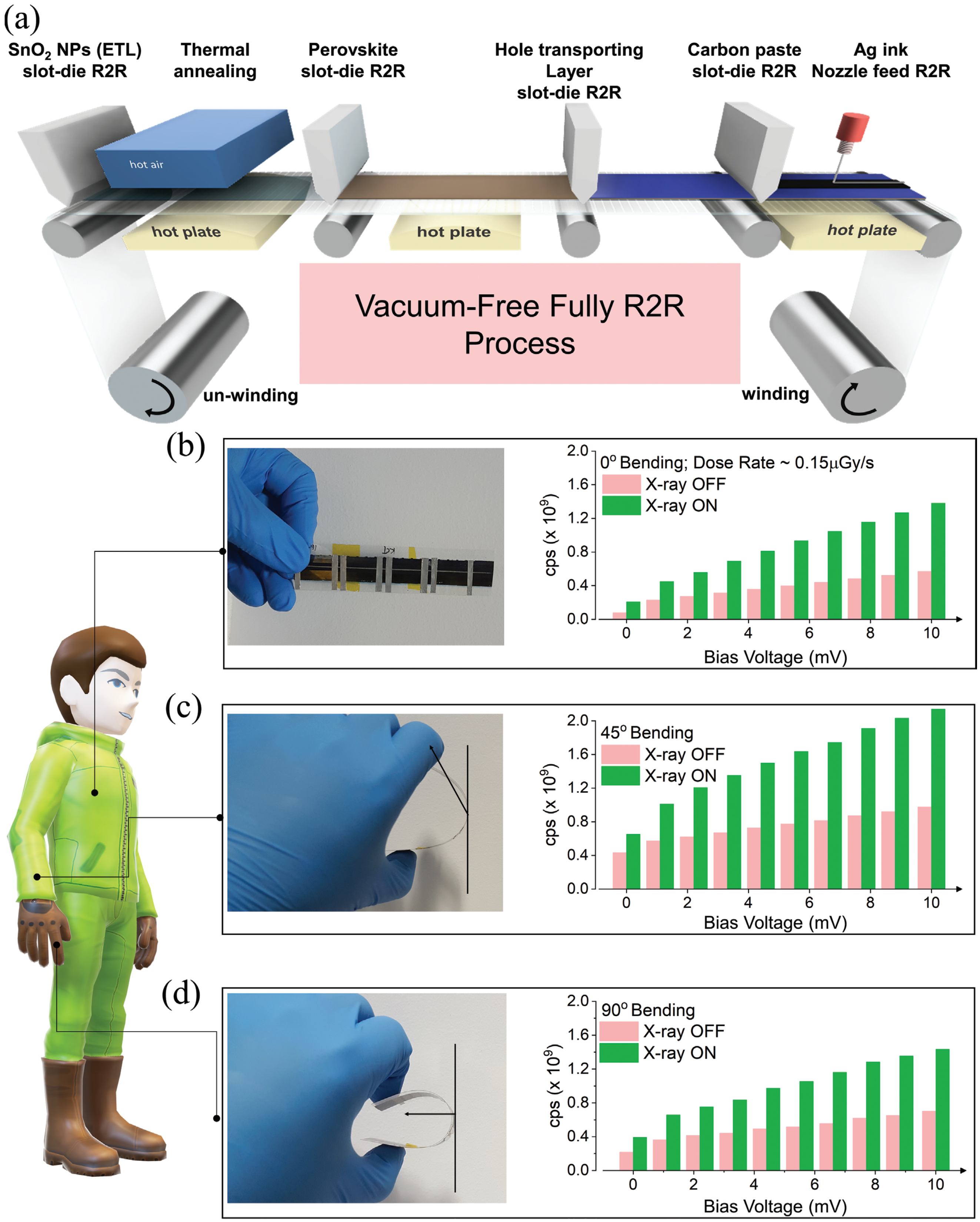

**Figure 5.** Printable, flexible, and scalable X-ray detectors. a) Schematic depiction of the fabrication process of an X-ray diode on flexible substrates using a custom-made slot die set up on a commercial R2R coater. The function of such a radiation detector at three potential areas on the human body are considered through notionally different bending positions, b) 0°, c) 45°, and d) 90°. The electrical signals under each bending condition are shown for different $V_{bias}$ for under X-ray OFF and ON (dose rate of 0.15 µGy $s^{-1}$) conditions.

30 s. Subsequently, the gold electrodes (20, 40, or 80 nm thickness) were thermally evaporated under a baseline pressure of less than $8 \times 10^{-6}$ Torr through a shadow mask.

*R2R Fabrication on the Flexible Substrate*: All the R2R experiments were carried under ambient conditions in a fume hood cabinet using a custom-made slot die setup on a commercial R2R coater (Mini-Labo, Yasui Seki). The coating speed was controlled by a built-in controller of the R2R coater while the solution flow through the slot die head was controlled by a syringe pump.

The 7.5 wt% of $SnO_2$ solution was slot die coated at 0.2 m $min^{-1}$ of coating rate with 12 µL $min^{-1}$ pumping rate, heated by passing under hot air at 130 °C, and annealed while passing a hot plate at 130 °C. For fast and continuous annealing for $SnO_2$, the film was annealed with in-line near-infrared radiation treatment at 90 °C with 30% of intensity at 0.9 m $min^{-1}$ of line speed through 5 m long oven. The film was then rewound to the starting point to coat perovskite solution. The 1 M of ACN/MA-based $MA_{0.875}FA_{0.125}PbI_3$ and 0.5 M of MABr added solution was pumped into slot die head. The slot die head was fed by tubing with an internal diameter of 0.3 mm and a length of 45 mm giving a dead volume of 78 µL. A syringe pump (neMESYS, CETONI) was used in this work with 2.5 mL Hamilton syringe (Sigma Aldrich). The perovskite solution with pump rate of 45 µL $min^{-1}$ was coated at 0.6 m $min^{-1}$ coating rate with 13 mm coating width under the room temperature. The gap between meniscus guide of slot-die head and substrate was set as 100–200 µm. The film was annealed while passing on the hot plate of 130 °C inline. After finishing the perovskite layer, the substrate was then rolled back as soon as possible and PPDT2FBT solution for HTL layer was coated at 0.42 m $min^{-1}$ of coating speed at room temperature with 32 µL $min^{-1}$ solution feed. Carbon electrode was deposited on HTL layer by slot-die with 5 mm width meniscus guide at 0.3 m $min^{-1}$ coating rate at 65 °C of coating bed. The Ag ink was simultaneously deposited with carbon by nozzle meniscus using syringe pump on 130 °C curved hot plate.

*Structural Characterizations*: The cross-sectional and top surface SEM images were obtained using a Magellan 400 FEG-SEM (FEI, USA) operated at 5 kV. XRD patterns were recorded with a Bruker D8 Advance Diffractometer with a Cu $K\alpha$ X-ray tube at 40 kV and 40 mA and with a step size of 0.02° and 0.8 s per step.

*X-Ray Detection Measurements*: The Monash X-ray Platform (MXP) and Australian synchrotron soft X-ray beamline (SXR) were used to achieve hard and soft X-ray detection, respectively. At MXP, the hard X-ray source of the D8 Discoverer was used to expose the devices (exposed area = 0.27 $cm^2$) in perfect dark conditions. The dose rate mapping at a device position was recorded by a portable Radiation Monitor Controller (Radical Corporation Model 9010). Dose rate was modulated by kV $mA^{-1}$ of the equipment and also by increasing the distance between a source and the device. The devices were then exposed to hard X-rays under the same equipment parameters and at ambient conditions. The photocurrent was extracted by the Keithley source-meter (2400 series). The sensitivity was calculated by using the slope of the drain current $I_{ds}$ versus dose rate plots for different thicknesses at fixed bias voltage (Figure S5b, Supporting Information).

Soft X-ray detection was achieved by exposing the diode device to Australian Synchrotron's soft X-rays with photon energies of between 100 eV and 2.5 keV and simultaneously recording the change in the device photocurrent. The soft X-ray beam at the Australian Synchrotron was adequately stable and possessed high intrinsic energy resolution to enable accurate assessment of a device. The n-i-p devices were placed on a custom-designed sample holder with a glass side attached to a sample holder through insulation sticky tape. The devices were pumped down to an ultrahigh vacuum environment, base pressure $1 \times 10^{-10}$ mbar. The synchrotron dose rate was controlled by changing the slit width and was calculated from the current measured by the standard photodiode. The *I–V* (current as a function of voltage) and *I–T* (current as a function of time) curves were recorded by Quick IV measurement software. Area of SXR beam 1 × 1 $mm^2$ was used to calculate the sensitivity.

*Analytical Simulations*: The simulations were performed in two stages: In the first stage, the incoming photon flux (dose rate) and power were used along with the Beer–Lambert law to calculate the carrier generation profile within the stack. The X-ray attenuation coefficients taken from the National Institute of Science and Technology (NIST) XCOM database were used to perform these calculations. In the second stage, the finite element and finite volume solvers of COMSOL Multiphysics were used to perform an electrical analysis of the system. Only the Spiro, $SnO_2$, and perovskite layers were simulated in the electrical solvers with ohmic boundary conditions at either end. Electron, hole, and ion drift-diffusion equations were solved for transient carrier densities and currents, finally solving for the current at the ohmic contact terminals. The thickness-dependent sensitivity was calculated using Mathematica and graphs were plotted using Python. The details are given in Section B in the Supporting Information.

## Supporting Information

Supporting Information is available from the Wiley Online Library or from the author.

## Acknowledgements

B.S. and J.C.Y. contributed equally to this work. This research was undertaken on a soft-X-ray beamline at the Australian Synchrotron, part of ANSTO. B.S. acknowledges funding support through Australian Synchrotron under reference number AS221/SXR/18131. J.J. acknowledges funding support through the Australian Research Council under Grant CE170100026 and the Australian-China Science and Research Fund Joint Research Centre for Flexible Graphene Electronics. N.M. and T.H. acknowledge funding from EPSRC (EP/L016087/1). The authors acknowledge the use of the facilities at the Monash Centre for Electron Microscopy (MCEM) and Monash X-ray Platform (MXP). The authors thank Dr. Bruce Cowie and Dr. Anton Tadich for developing a home-built sample holder and assistance in experiments at Synchrotron. The authors thank Dr. Bin Li (Monash University) for collecting SEM images. The authors also thank Dr. Muhammad Nadeem (University of Wollongong) for helpful discussions.

Open access publishing facilitated by Monash University, as part of the Wiley - Monash University agreement via the Council of Australian University Librarians.

## Conflict of Interest

The authors declare no conflict of interest.

## Data Availability Statement

The data that support the findings of this study are available on request from the corresponding author. The data are not publicly available due to privacy or ethical restrictions.

## Keywords

direct detection, dual energy detection, flexible substrate, metal halide perovskite, roll-to-roll printing, X-ray detector

Received: October 31, 2022
Revised: February 13, 2023

[1] a) *Nature* **1896**, *53*, 274; b) W. H. Bragg, *Nature* **1912**, *90*, 219.
[2] P. Allisy-Roberts, J. Williams, *Farr's Physics for Medical Imaging*, 2nd ed., Elsevier, New York **2007**.
[3] C. H. McCollough, S. Leng, L. Yu, J. G. Fletcher, *Radiology* **2015**, *276*, 637.
[4] R. Garnett, *Clin. Imaging* **2020**, *67*, 160.
[5] a) D. A. Scaduto, O. Tousignant, W. Zhao, *Med. Phys.* **2017**, *44*, 3965; b) N. Allec, S. Abbaszadeh, A. Fleck, O. Tousignant, K. S. Karim, *IEEE Trans. Nucl. Sci.* **2012**, *59*, 1856.
[6] D. Mortensen, *Thickness Dependence of Electron Transport in Amorphous Selenium for Use in Direct Conversion Flat Panel X-ray Detectors*, University of Saskatchewan, **2012**.
[7] a) H. Wei, J. Huang, *Nat. Commun.* **2019**, *10*, 1066; b) Y. Liu, Z. Xu, Z. Yang, Y. Zhang, J. Cui, Y. He, H. Ye, K. Zhao, H. Sun, R. Lu, M. Liu, M. G. Kanatzidis, S. Liu, *Matter* **2020**, *3*, 180; c) S. Shrestha, R. Fischer, G. J. Matt, P. Feldner, T. Michel, A. Osvet, I. Levchuk, B. Merle, S. Golkar, H. Chen, S. F. Tedde, O. Schmidt, R. Hock, M. Rührig, M. Göken, W. Heiss, G. Anton, C. J. Brabec, *Nat. Photonics* **2017**, *11*, 436; d) S. Yakunin, M. Sytnyk, D. Kriegner, S. Shrestha, M. Richter, G. J. Matt, H. Azimi, C. J. Brabec, J. Stangl, M. V. Kovalenko, W. Heiss, *Nat. Photonics* **2015**, *9*, 444; e) H. Wei, Y. Fang, P. Mulligan, W. Chuirazzi, H.-H. Fang, C. Wang, B. R. Ecker, Y. Gao, M. A. Loi, L. Cao, J. Huang, *Nat. Photonics* **2016**, *10*, 333; f) S. Yakunin, D. N. Dirin, Y. Shynkarenko, V. Morad, I. Cherniukh, O. Nazarenko, D. Kreil, T. Nauser, M. V. Kovalenko, *Nat. Photonics* **2016**, *10*, 585; g) Y. C. Kim, K. H. Kim, D.-Y. Son, D.-N. Jeong, J.-Y. Seo, Y. S. Choi, I. T. Han, S. Y. Lee, N.-G. Park, *Nature* **2017**, *550*, 87.
[8] H. Wu, Y. Ge, G. Niu, J. Tang, *Matter* **2021**, *4*, 144.
[9] a) Y. Zhou, J. Chen, O. M. Bakr, O. F. Mohammed, *ACS Energy Lett.* **2021**, *6*, 739; b) H. Tsai, F. Liu, S. Shrestha, K. Fernando, S. Tretiak, B. Scott, D. T. Vo, J. Strzalka, W. Nie, *Sci. Adv.* **2020**, *6*, eaay0815; c) H. M. Thirimanne, K. D. G. I. Jayawardena, A. J. Parnell, R. M. I. Bandara, A. Karalasingam, S. Pani, J. E. Huerdler, D. G. Lidzey, S. F. Tedde, A. Nisbet, C. A. Mills, S. R. P. Silva, *Nat. Commun.* **2018**, *9*, 2926; d) J. Pang, S. Zhao, X. Du, H. Wu, G. Niu, J. Tang, *Light: Sci. Appl.* **2022**, *11*, 105.
[10] L. M. Herz, *ACS Energy Lett.* **2017**, *2*, 1539.
[11] B. Charles, M. T. Weller, S. Rieger, L. E. Hatcher, P. F. Henry, J. Feldmann, D. Wolverson, C. C. Wilson, *Chem. Mater.* **2020**, *32*, 2282.
[12] M. J. Berger, XCOM: Photon Cross Sections Database: NIST Standard Reference Database 8 (NIST), **2013**.
[13] A. Alagumalai, M. Venu Rajendran, S. Ganesan, V. Sudhakaran Menon, R. K. Raman, S. M. Chelli, S. Muthukumar Vijayasayee, S. A. Gurusamy Thangavelu, A. Krishnamoorthy, *ACS Appl. Energy Mater.* **2022**, *5*, 6783.
[14] S. Kasap, J. B. Frey, G. Belev, O. Tousignant, H. Mani, J. Greenspan, L. Laperriere, O. Bubon, A. Reznik, G. DeCrescenzo, K. S. Karim, J. A. Rowlands, *Sensors* **2011**, *11*, 5112.
[15] a) H. Mescher, E. Hamann, U. Lemmer, *Sci. Rep.* **2019**, *9*, 5231; b) M. Z. Kabir, S. O. Kasap, *Appl. Phys. Lett.* **2002**, *80*, 1664.
[16] W. Rehman, D. P. McMeekin, J. B. Patel, R. L. Milot, M. B. Johnston, H. J. Snaith, L. M. Herz, *Energy Environ. Sci.* **2017**, *10*, 361.
[17] Q. Dong, Y. Fang, Y. Shao, P. Mulligan, J. Qiu, L. Cao, J. Huang, *Science* **2015**, *347*, 967.
[18] M. C. Gélvez-Rueda, N. Renaud, F. C. Grozema, *J. Phys. Chem. C* **2017**, *121*, 23392.
[19] Y. Zhou, L. Zhao, Z. Ni, S. Xu, J. Zhao, X. Xiao, J. Huang, *Sci. Adv.* **2021**, *7*, eabg6716.
[20] T. Dinh, T. Nguyen, H.-P. Phan, V. Dau, D. Dao, N.-T. Nguyen, *Reference Module in Biomedical Sciences*, Elsevier, New York **2021**.
[21] W. Wei, Y. Zhang, Q. Xu, H. Wei, Y. Fang, Q. Wang, Y. Deng, T. Li, A. Gruverman, L. Cao, J. Huang, *Nat. Photonics* **2017**, *11*, 315.
[22] B. Shabbir, J. Liu, V. Krishnamurthi, R. A. W. Ayyubi, K. Tran, S. A. Tawfik, M. M. Hossain, H. Khan, Y. Wu, B. N. Shivananju, R. U. R. Sagar, A. Mahmood, A. Younis, M. H. Uddin, S. A. Bukhari, S. Walia, Y. Li, M. J. S. Spencer, N. Mahmood, J. J. Jasieniak, *Adv. Funct. Mater.* **2022**, *32*, 2105038.
[23] a) Y. Li, J. Liu, X. Su, Q. Ou, Z. Wan, Y. Wu, W. Yu, X. Bao, Y. Huang, X. Wang, A. Tadich, B. Shabbir, Q. Bao, *J. Mater. Chem. C* **2020**, *8*, 6659; b) J. Liu, B. Shabbir, C. Wang, T. Wan, Q. Ou, P. Yu, A. Tadich, X. Jiao, D. Chu, D. Qi, D. Li, R. Kan, Y. Huang, Y. Dong, J. Jasieniak, Y. Zhang, Q. Bao, *Adv. Mater.* **2019**, *31*, 1901644; c) Q. Lin, S. Bernardi, B. Shabbir, Q. Ou, M. Wang, W. Yin, S. Liu, A. S. R. Chesman, S. O. Fürer, G. Si, N. Medhekar, J. Jasieniak, A. Widmer-Cooper, W. Mao, U. Bach, *Adv. Funct. Mater.* **2022**, *32*, 2109442.
[24] A. Vilouras, A. Christou, L. Manjakkal, R. Dahiya, *ACS Appl. Electron. Mater.* **2020**, *2*, 2601.
[25] X. Liang, C. Ge, Q. Fang, W. Deng, S. Dey, H. Lin, Y. Zhang, X. Zhang, Q. Zhu, H. Hu, *Front. Mater.* **2021**, *8*, 634353.